Critical dynamics of a two-dimensional superfluid near a nonthermal fixed point

Jan Schole, Boris Nowak,* and Thomas Gasenzer†

Institut für Theoretische Physik, Ruprecht-Karls-Universität Heidelberg, Philosophenweg 16, 69120 Heidelberg, Germany and ExtreMe Matter Institute EMMI, GSI Helmholtzzentrum für Schwerionenforschung GmbH, Planckstraße 1, 64291 Darmstadt, Germany

(Received 20 April 2012; published 17 July 2012)

Critical dynamics of an ultracold Bose gas far from equilibrium is studied in two spatial dimensions. Superfluid turbulence is created by quenching the equilibrium state close to zero temperature. Instead of immediately rethermalizing, the system approaches a meta-stable transient state, characterized as a nonthermal fixed point. A focus is set on the vortex density and vortex-antivortex correlations which characterize the evolution towards the nonthermal fixed point and the departure to final (quasi-)condensation. Two distinct power-law regimes in the vortex-density decay are found and discussed in terms of a vortex unbinding process and a kinetic description of vortex scattering. A possible relation to decaying turbulence in classical fluids is pointed out. By comparing the results to equilibrium studies of a two-dimensional Bose gas, an intuitive understanding of the location of the nonthermal fixed point in a reduced phase space is developed.

DOI: 10.1103/PhysRevA.86.013624 PACS number(s): 03.75.Kk, 03.75.Lm, 47.27.E−, 67.85.De

I. INTRODUCTION

Generically, the properties of an interacting many-body system far from equilibrium can change violently in time. This is not the case, however, when the system reaches a nonthermal fixed point (NTFP). In the vicinity of such a fixed point the dynamics is expected to slow down, and correlation functions to exhibit universal scaling behavior. Such transient states have been intensively studied in the context of classical turbulence [1–4]. Similar phenomena appear in degenerate quantum many-body systems, e.g., in superfluid helium or dilute ultracold quantum gases, where superfluid or quantum turbulence (QT) has been discussed in great detail [5–12]. More general types of turbulence, so-called wave turbulence, have been studied [13,14], mainly in the framework of kinetic theory. Recent applications include far-from-equilibrium quantum systems, such as dilute ultracold Bose gases [15–25], the inflating and reheating early universe [26–30], and quark-gluon matter created in heavy-ion collisions [31–37]. Thereby, an extension of kinetic wave turbulence by nonperturbative quantum-field-theory methods lead to the notion of a NTFP [27,28,30,33], in analogy to fixed points describing equilibrium as well as dynamical critical phenomena [38].

It was demonstrated in Refs. [16,24] that in a two- or three-dimensional superfluid Bose gas, such an NTFP is realized by a state with a dilute random distribution of vortices or vortex lines, respectively, of both positive and negative circulation. This gave the relation to QT [5–9,14] as well as a link between weak wave turbulence described by kinetic theory and topological excitations in nonlinear wave systems.

In this paper, we study the nonequilibrium dynamics of a two-dimensional Bose gas evolving towards and away from an NTFP, the stationary properties of which were discussed in Refs. [15,16,24]. In this process the appearance and decay of vortex excitations play a crucial role. We monitor the vortex density during equilibration of the turbulent gas and reveal a bimodal scaling behavior in time. By following vortex-antivortex correlations, we show that this phenomenon is directly related to a nonequilibrium vortex unbinding process. Ultimately, vortex excitations evolve into an almost-random distribution which constitutes the universal scaling at the NTFP.

In contrast to classical turbulence, the decay of superfluid turbulence is typically accompanied by a buildup of coherence and quasicondensation [17–22,42,43]. In Fig. 1 we sketch the projection of this process onto the space spanned by the coherence length l_C and the mean intervortex pair distance l_D. In this way, the dynamical evolution towards and away from a NTFP can be compared to the properties of near-equilibrium states of a two-dimensional degenerate Bose gas [39–41,44–46]. Arrows mark the direction of the flow and

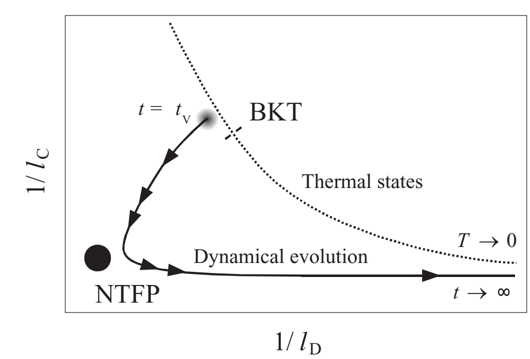

FIG. 1. Dynamical evolution of a two-dimensional superfluid near a nonthermal fixed point (NTFP). The sketch shows the equilibration process after a quench, in the space of inverse coherence length l_C and inverse mean vortex-antivortex pair distance l_D. The "dynamical evolution" illustrates trajectories of decaying superfluid turbulence starting from the time at which vortices appear, $t = t_V$, approaching the NTFP, and, finally, evolving towards equilibrium. The line labeled "thermal states" qualitatively illustrates these quantities for thermal configurations [39–41], featuring a steady decrease in inverse coherence with inverse mean vortex-antivortex distance and including a Berezinskii-Kosterlitz-Thouless (BKT) phase transition. An unbinding of vortices of opposite circulation characterizes the approach to the NTFP before, finally, all vortices decay, $l_D \to 0$, to establish equilibrium phase coherence, here at a temperature below the BKT transition.

*b.nowak@thphys.uni-heidelberg.de
†t.gasenzer@uni-heidelberg.de

indicate that critical slowing down occurs near the NTFP. An unbinding of vortices of opposite circulation occurs during the approach of the fixed point before, finally, all vortices decay to establish full equilibrium phase coherence.

Metastable multivortex states—or, in one spatial dimension, solitary waves—are also known to appear from strong fluctuations in the vicinity of the normal fluid–to–superfluid transition. Crossing such a transition by varying an equilibrium macroscopic parameter like the temperature at a certain rate is well known to induce defect creation. Their number depends on the coherence length at the point where the parameter variation ceases to be adiabatic [47,48]. Experiments with ultracold Bose gases following such Kibble-Zurek-type protocols [49,50] as well as generating superfluid turbulence [10,11] are pursued with increasing effort and could serve to discover and study systematically NTFPs.

Turbulence has served, since the seminal work of Kolmogorov [2–4], as one of the first phenomena to develop renormalization-group (RG) techniques out of equilibrium. The effectively local transport processes in momentum, i.e., scale space, which are at the basis of turbulent cascades immediately suggest themselves for an RG analysis [51]. For two-dimensional ultracold gases, the dynamical evolution in the vicinity of the Berezinskii-Kosterlitz-Thouless (BKT) critical point [45,46] was studied in Refs. [52], also in terms of a perturbative RG analysis. For early work see [38] and references cited therein. A more general set of perturbative nonequilibrium RG equations for the one-dimensional sine-Gordon model near the Luttinger-liquid fixed point was derived in [53], and the route to a nonperturbative analysis also for the strong-coupling regime is provided by out-of-equilibrium functional RG techniques [54–56] which will be followed in a forthcoming paper.

II. DYNAMICAL SIMULATIONS

In this paper we focus on the dynamical evolution of a two-dimensional dilute Bose gas towards an NTFP and away from it to thermal equilibrium. We statistically simulate the far-from-equilibrium dynamics in the classical-wave limit of the underlying quantum field theory. The classical equation of motion for the complex scalar field $\phi(\mathbf{x},t)$ reads

$$i\partial_t\phi(\mathbf{x},t) = \left[-\frac{\nabla^2}{2m} + g|\phi(\mathbf{x},t)|^2\right]\phi(\mathbf{x},t). \quad (1)$$

Here, m is the boson mass, g quantifies the interaction strength in $d = 2$ dimensions, and, in our units, $\hbar = 1$. Our computations are performed in a computational box of size L^2 on a grid with side length $L = N_s a_s$, lattice spacing a_s, and periodic boundary conditions. We define the dimensionless variables $\overline{g} = 2mg$, $\overline{t} = t/\tau$, with lattice time unit $\tau = 2ma_s^2$ and $\overline{\psi}_n(t) = \psi_n a_s \exp(2i\overline{t})$; see [24] for further details. All simulations are performed with parameters $\overline{g} = 3\times10^{-5}$ and $N/N_s^2 = 1525$, where N is the total number of particles. When appropriate, we express length scales in units of the healing length $\xi = (2mgN/L^2)^{-1/2} = 4.6\,a_s$. We drop overbars in the following. We choose initial states with a few macroscopically occupied modes in momentum space, as illustrated in Fig. 2. Fluctuations around these mean values are introduced by sampling the initial field modes according to Gaussian Wigner distributions. Such statistical simulations, also done under the name truncated Wigner approach, are quasiexact in the classical wave regime of macroscopic occupation numbers. The type of initial conditions shown in Fig. 2 induces transport of particles and energy, which leads to vortex creation and turbulence. These field configurations describe quenched superfluid states, which can, for instance, be prepared by Bragg scattering of photons from a (quasi-)condensate. By varying the number and geometry of initially occupied modes, we can probe the initial-state dependence of our observables.

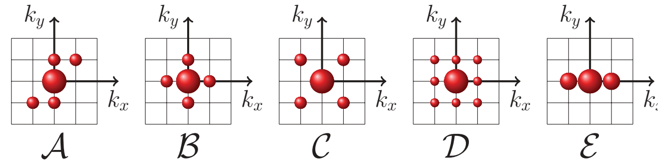

FIG. 2. (Color online) $\mathcal{A}$–$\mathcal{E}$ illustrate the initially occupied momentum modes $\mathbf{k}_{\rm ini}$ (shaded spheres) with $n(\mathbf{k}_{\rm ini},t=0) \gg 1$, for five mean-field configurations. The areas of the spheres are proportional to the mean numbers of particles. A sixth initial condition, $\mathcal{A}^*$, is geometrically the same as $\mathcal{A}$, but with initially occupied momenta $\mathbf{k}^*_{\rm ini} = 4\mathbf{k}_{\rm ini}$. If not stated otherwise, on average, half of the total number of particles occupies the zero mode.

A. Creation of vortices and turbulence

In the presence of a nonvanishing coupling g the initial states depicted in Fig. 2 are far from thermal equilibrium. During the first stages of the evolution coherent scattering into higher excited modes dominates. In Fig. 3 (left), we show

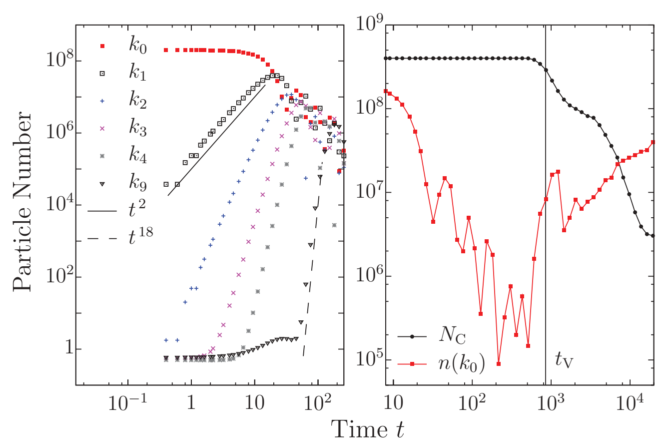

FIG. 3. (Color online) Left: Single-particle occupation numbers $n(\mathbf{k},t) = \langle|\phi(\mathbf{k},t)|^2\rangle$ as a function of time t (in lattice units), for different discrete momentum modes $\mathbf{k} = (k_n,0)$, $k_n = 2\sin(n\pi/N_s)$, along the k_x axis. Results are computed on a grid of size $N_s = 512$, from initial field configuration $\mathcal{A}$. Note the double-logarithmic scale. Lines show different power-law evolutions $\sim t^{2n}$. Right: Zero-mode occupation number $n((k_0,0),t)$ and coherent population $N_C = \int d^2x|\langle\phi(\mathbf{x},t)\rangle|^2$ as a function of time t (double-log scale), for an average over 100 runs, grid size $N_s = 512$, and initial condition $\mathcal{A}$. t_V marks the time of vortex creation.

the time evolution of the ensemble-averaged single-particle momentum occupation numbers $n(\mathbf{k},t) = \langle|\phi(\mathbf{k},t)|^2\rangle$ as a function of time, for several momenta $\mathbf{k} = (k_i,0)$ along the k_x axis. One observes a power-law growth of momenta with $k_x > 0$ until $t \simeq 10^2$. This process, exhibiting fast power-law growth $\sim t^{2n}$ of occupations can be understood from analytic mean-field calculations by approximating strong initial occupations to be time independent. It is present for all our initial conditions and independent of spatial dimension.

In Fig. 3 (right), we continue to follow the time evolution of the condensate mode, $n(0,t)$. The decay of the zero-mode occupation is part of a nonlocal energy and particle transport to higher momenta. In coordinate space, this process leads to the formation of shock waves, which decay into large numbers of vortices (see Ref. [24] and videos of the evolution [57]). In addition, we study the coherent population $N_C = \int d^2x\,|\langle\phi(\mathbf{x},t)\rangle|^2$ for an initially phase-coherent ensemble $N_C(t=0) = N$. The dynamics preserve coherence until vortices form around time $t = t_V \simeq 10^3$. This can be understood by considering that the local phase angle $\varphi(\mathbf{x},t)$ of the complex field $\phi = |\phi|\exp\{i\varphi\}$ is determined by the positions of the vortices. Since vortices interact strongly, their trajectories in position space quickly randomize. Hence, in the ensemble average the coherent population decays. Beyond this time, density fluctuations are significant only at momenta larger than the inverse healing length, $k > 1/\xi$, whereas long-range fluctuations of the Bose gas are dominated by vortical flow. For $t \gtrsim t_V$, the zero-mode population $n(0,t)$ starts to increase, signaling the onset of phase ordering associated with vortex annihilations. This process is studied in the following sections.

B. Vortex density decay

After the creation of vortices, the dynamical evolution exhibits a dual cascade in momentum space, transporting particles from intermediate to small momenta and energy from intermediate to large momenta [24]. The single-particle momentum spectrum develops a quasistationary bimodal scaling, with characteristic exponents corresponding to the respective cascade processes. The system approaches an NTFP [15,24]. The low-momentum scaling of the single-particle momentum distribution can be related to the presence of randomly distributed vortices and antivortices [24]. In the present article, the evolution towards and away from the NTFP is investigated. First, we show that the approach to the NTFP is accompanied by a change of the characteristic scaling of the ensemble averaged vortex density $\rho(t)$ with time.

Figure 4(a) shows the time evolution of the vortex density

$$\rho(t) = \langle N^{V}(t) + N^{A}(t)\rangle / V, \qquad (2)$$

with $N^{V(A)}(t)$ being the number of vortices (antivortices) in volume V at time t, found in simulations starting from the initial conditions defined in Fig. 2. Vortices are counted by detecting their characteristic density and phase profiles. In all runs, vortex formation occurs around $t_V \simeq 10^3$, apparent from the steep increase in vortex density around this time. For $t \gtrsim t_V$, two distinct stages in the vortex density decay are observed, a rapid early stage and a slow late stage. Specifically, the vortex density follows power laws $\rho(t) \sim t^{-\alpha_i}$ with two different exponents α_i, $i = 1,2$. The exponent during the early stage depends considerably on initial conditions $1 \lesssim \alpha_1 \lesssim 2$, whereas the late stage features a decay exponent in a narrow interval, $0.3 \lesssim \alpha_2 \lesssim 0.4$. From our analysis given in Sec. II G, we estimate that the closest approach to the NTFP is reached at $t \simeq (5\text{–}10) \times 10^5$.

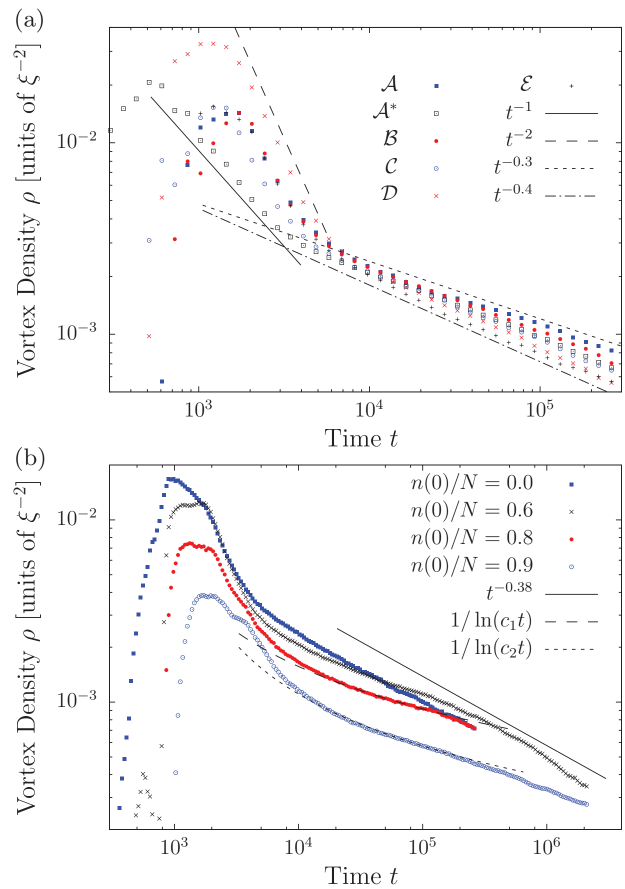

FIG. 4. (Color online) Vortex density ρ as a function of time t (in lattice units). Note the double-logarithmic scale. (a) Evolution for various initial conditions as given in Fig. 2, averaged over 20 runs on a grid of size $N_s = 1024$. Lines show different power-law evolutions. Assuming the area of a vortex to be given by $V_V = (2\xi)^2\pi$, a maximally dense packing of vortices would correspond to the vortex density $\rho_{max} = 1/V_V = 1/(4\pi\xi^2)$. (b) Evolution for different initial zero-mode populations $n(0)/N$. Averages were taken over 20 runs on a lattice of size $N_s = 1024$, for initial condition $\mathcal{A}$. Fitted parameters are $c_1 = 0.0026$ and $c_2 = 0.0012$. The closest approach to the NTFP is reached at $t \simeq (5\text{–}10) \times 10^5$.

We have repeated our simulations on various grid sizes, $N_s \in \{256,512,1024,4096\}$. Thereby, we found that decay exponents saturate for and above $N_s = 512$. We attribute deviations on smaller grids to effects from regular (integrable) dynamics of few-vortex systems [58]. We remark that the onset of the slow decay coincides with the development of a particular scaling behavior in the single-particle momentum distribution $n(k) \sim k^{-4}$, which in Refs. [15,16,24] was shown to signal the approach to the NTFP and the formation of a set of randomly distributed vortices. In this context, the reduction of the vortex density decay exponent, compared to the early stage of rapid decay, is interpreted as a (critical) slowing-down of the nonlinear dynamics near the NTFP.

As shown in Fig. 4(b), the vortex density decay at late times is not always given by a power law. By considerably increasing the initial population of the zero mode, e.g., $n(0)/N \in \{0.6,0.8,0.9\}$, we find that for some time the vortex density is better described by an inverse-ln function $\rho(t) \sim 1/\ln(t)$. However, at late times $t \gtrsim t^*$, the decay seems to converge to a power law from the slow-decay regime. By analyzing the dynamics of the single-particle momentum distribution, we could identify the time t^* to be the time when compressible excitations have thermalized the high-momentum tail of the spectrum (for details see Fig. (10) in Ref. [24]). This is consistent with the observation that the inverse-ln decay could not be observed for initial conditions with small zero-mode occupation, where high-momentum thermalization happens more rapidly.

C. Vortex correlations

In the following, the dynamical transition in the vortex annihilation dynamics is discussed in terms of characteristic features of the vortex-antivortex correlation function

$$g_{\mathrm{VA}}(\mathbf{x},\mathbf{x}',t) = \frac{\langle \rho^{\mathrm{V}}(\mathbf{x},t)\rho^{\mathrm{A}}(\mathbf{x}',t)\rangle}{\langle \rho^{\mathrm{V}}(\mathbf{x},t)\rangle\langle \rho^{\mathrm{A}}(\mathbf{x}',t)\rangle}, \tag{3}$$

where $\rho^{\mathrm{V(A)}}(\mathbf{x},t) = \sum_i \delta(\mathbf{x} - \mathbf{x}_i(t))$ is the distribution of vortices (antivortices) at time t in a single run. For sufficiently large ensembles, g_{VA} is a function of $r = |\mathbf{x} - \mathbf{x}'|$ only.

In Fig. 5(a), we show the evolution of $g_{\mathrm{VA}}(r,t)$ as a function of r for different times during the fast-decay stage. At early times, one finds a strong pairing peak near $r = 0$. This peak is quickly reduced and a hole is "burned" into the correlation function near the origin [see Fig. 5(b)]. Following the time evolution of the spatial vortex distribution, we observe that this involves qualitatively different processes: Mutual annihilations of closely positioned vortices and antivortices occur under the emission of sound waves. Further separated vortices can approach each other in different ways as illustrated in Fig. 6. The scattering of two pairs can directly lead to the annihilation of one pair under the emission of sound waves. We consider this to include events where the pair distance of one dipole reduces below a certain threshold, so that it looks like a density dip rather than a vortex pair. This density dip can still interact with other vortices, but it will quickly vanish. Alternatively, the scattering reduces the vortex-antivortex separation within one pair, while it increases it within the other, in accordance with the Onsager point-vortex model [44]. We refer to this characteristic change in $g_{\mathrm{VA}}(r)$ as a vortex unbinding process. The scattering of a closely bound vortex off an isolated vortex is not shown, because it is included as a collision between a closely and a loosely bound pair. At around the time $t_3 \lesssim t \lesssim t_4$ the power-law exponent of the vortex density decay changes to about a third of its previous value [see inset in Fig. 5(a)]. Next, we compute the mean vortex-antivortex pair distance l_{D}, by averaging over distances between each vortex and its nearest antivortex. In accordance with the previous discussion, l_{D} grows continuously, exhibiting two characteristic stages [see inset in Fig. 5(b)]. At times $t \gtrsim 10^4$, $l_{\mathrm{D}}(t)$ approaches the power-law solution $l_{\mathrm{D}} \sim \rho^{-1/2}$, as expected for uncorrelated vortices.

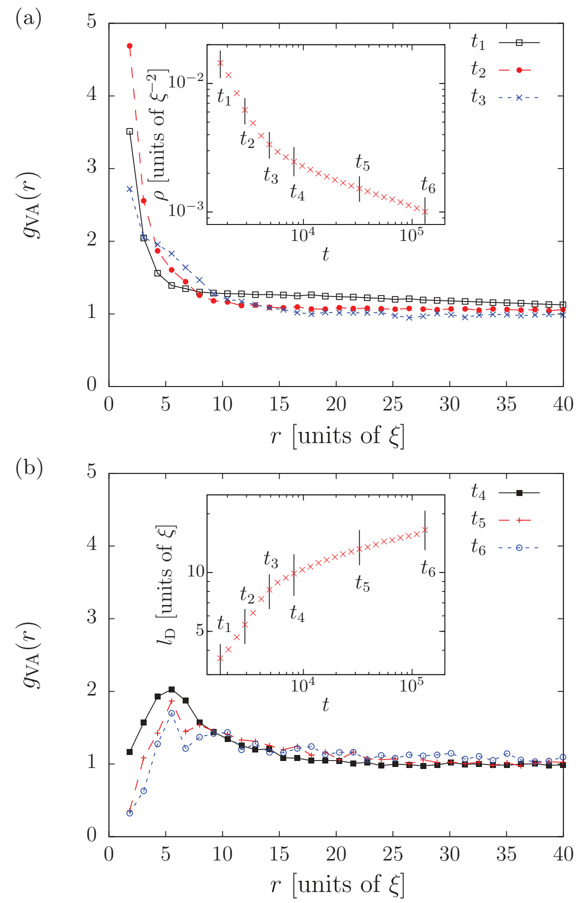

FIG. 5. (Color online) Normalized vortex-antivortex correlation functions g_{VA} defined in Eq. (3) as a function of radial coordinate r, for six times, t_i (in lattice units). (a) $g_{\mathrm{VA}}(r)$ at times t_i, $i = 1,2,3$, during the rapid-decay stage, averaged over 174 runs on a grid of size $N_s = 1024$, using initial condition $\mathcal{A}$. Inset: Vortex density ρ as a function of time t, taken from the simulations for Fig. 4(a). (b) $g_{\mathrm{VA}}(r)$ at times t_i, $i = 4,5,6$, during the slow-decay stage, averaged over 174 runs on a grid of size $N_s = 1024$, using initial condition $\mathcal{A}$. Inset: Mean vortex-antivortex pair distance l_{D} as a function of time, from the simulations for Fig. 4(a).

D. Energy equilibration

The main result of the previous section is the relation of different stages in the evolution of the vortex density $\rho(t)$ to characteristic features in the vortex-antivortex correlation function $g_{\mathrm{VA}}(r,t)$. The vortex density decay was shown to be accompanied by a dynamical vortex unbinding. This finding can be supplemented by considering the evolution of different energies contained in the gas. In Refs. [5,59] it was suggested to decompose the kinetic energy into an incompressible and a compressible component, which, for conciseness, we give details of in the Appendix. In this way, contributions from vortical excitations can be separated from other excitations such as sound waves. In Fig. 7, we show the time evolution of different energy components for initial condition $\mathcal{A}$. One observes that the decay of the incompressible energy can be estimated to follow a power law $\sim t^{-1.25}$ during the early-time stage and $\sim t^{-0.2}$ in the late-time stage. This decay happens considerably more slowly than the vortex density decay in the early-time (late-time) stage, $\sim t^{-1.7}(\sim t^{-0.3})$, discussed in

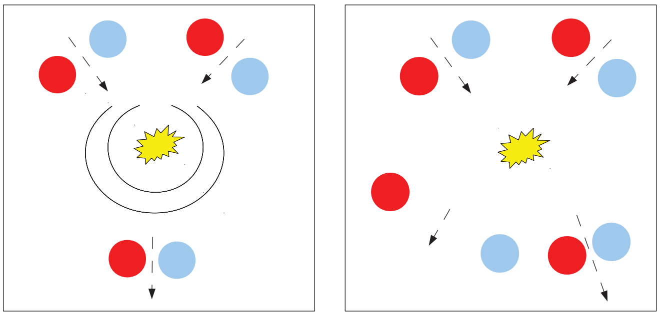

FIG. 6. (Color online) Sketch of scattering events between two vortex-antivortex pairs in $d = 2$ dimensions. Left: Scattering of two vortex pairs resulting in the mutual annihilation of two vortices and the emission of density waves. Right: Scattering of two vortex pairs, leading to a change in the vortex-antivortex distance l_D and pair velocity $\bar{v}$. We remark that once $l_D \sim \xi$, a vortex pair decays rapidly under the emission of density waves.

Sec. II B. As a result, the incompressible energy per vortex grows as $\sim t^{0.45}$ at early times and as $\sim t^{0.1}$ at late times. Since the energy of a vortex pair increases with distance, this is in agreement with the phenomenon of increasing vortex-antivortex pair distance l_D.

At late times, compressible and quantum-pressure energy components develop into an equipartitioned state, also observed in decaying superfluid turbulence starting from a Taylor-Green vortex configuration [60].

E. Possible relation to classical turbulence in $d = 2$ dimensions

In the following, we discuss a similarity between our results and findings in classical fluid turbulence. Great efforts have been made to investigate freely decaying turbulence in two-dimensional classical fluids, see, e.g., Refs. [62–69]. In this context, special focus was set on the decay of the enstrophy

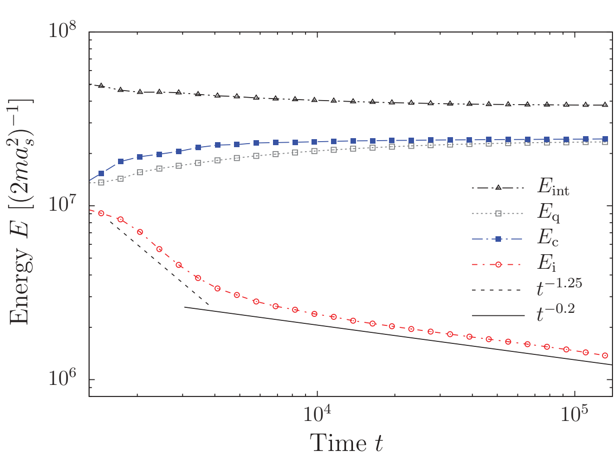

FIG. 7. (Color online) Contributions to the total energy as functions of time t (in lattice units), averaged over 174 runs. We show the interaction energy $E_{\rm int}$, compressible energy $E_{\rm c}$, incompressible energy $E_{\rm i}$, and quantum pressure $E_{\rm q}$, as defined in the Appendix, derived on a grid of size $N_s = 1024$ and for initial condition $\mathcal{A}$ defined in Fig. 2. Note the double-logarithmic scale. See Sec. II D for a discussion of the power-law evolutions.

$\Omega(t)$, which is related to the vorticity $\omega = \nabla \times \mathbf{v}$ of the velocity field $\mathbf{v}(\mathbf{x},t)$ by

$$\Omega(t) = \frac{1}{2}\int d^2x\, |\omega(\mathbf{x},t)|^2. \tag{4}$$

It was found by different methods that the long-time decay of the enstrophy is given by a power-law $\Omega(t) \sim t^{-\gamma}$, with $\gamma \simeq 0.35$–0.4 [62–69].

In superfluids, vorticity is concentrated in the vortex cores. The vorticity of a turbulent flow consisting of M vortices with circulations κ_i and positions $\mathbf{x}_i$, for $i < M$, is given by $\omega(\mathbf{x},t) = \sum_i \kappa_i \delta(\mathbf{x} - \mathbf{x}_i(t))$. Hence, in a flow consisting of vortices with circulations $\kappa_i = \pm 1$ the enstrophy reads

$$\Omega(t) = \tfrac{1}{2}\delta(\mathbf{0})M(t), \tag{5}$$

which is, with $\delta(\mathbf{0}) \sim 1/V$, proportional to the vortex density, $\Omega(t) \propto \rho(t)$. As shown in Fig. 4(a), in the late-time stage, our results are in accordance with the results from classical turbulence. However, we point out that the mechanisms of enstrophy decay in the two systems are fundamentally different. Whereas in superfluids vortices annihilate, the main process of vorticity decay in classical two-dimensional fluids is the merging into larger vortices.

We, finally, remark that in numerical simulations of freely decaying classical turbulence, a crossover between two stages of power-law decay similar to our findings has been reported in Ref. [69].

F. Kinetic theory of vortex scattering

The decay of the vortex density has been investigated in two-dimensional classical fluids [62–69] and superfluids [43,70–72], mainly in the presence of driving or dissipation. Several authors have proposed kinetic theories building on assumptions about the decay process [61,62,67,68]. The vortex decay cannot be explained by a simple model of independent vortices and antivortices moving towards each other to minimize the energy. Neglecting interactions with sound waves, vortex-antivortex pairs perform a collective motion perpendicular to their relative distance vector without changing their distance. This motion quickly leads to pair-pair collisions and establishes a kinetic-theory picture for vortex pairs. In Fig. 6, we show two examples of vortex-pair scattering processes altering the vortex density $\rho(t)$ and vortex correlation functions $g_{\rm VA}(r,t)$.

Assuming that the vortices are moving in pairs and that annihilations happen as the result of collisions of vortex pairs, the decay rate for the number $N_{\rm V}$ of vortices follows from the number of dipoles $N_{\rm D} \sim N_{\rm V}$ and $\partial_t N_{\rm D}(t) \sim -N_{\rm D}(t)/\tau$, with mean free collision time τ. The mean free collison time $\tau = l_{\rm mfp}/\bar{v}$ is given by the mean velocity of the pairs $\bar{v}$ and the mean free path $l_{\rm mfp} = V/(\sigma N_{\rm D})$ with cross section σ. Both the mean velocity and the cross section depend on the number of vortices via the mean vortex-antivortex pair distance $l_{\rm D}$ according to $\bar{v} \sim 1/l_{\rm D}$ and $\sigma \sim l_{\rm D}$. These considerations result in a rate equation,

$$\partial_t N_{\rm V}(t) = -cN_{\rm V}^2/\tau, \tag{6}$$

with dimensionless constant c. Equation (6) has the power-law solution $N_{\rm V}(t) \sim t^{-1}$. This decay law can only be observed

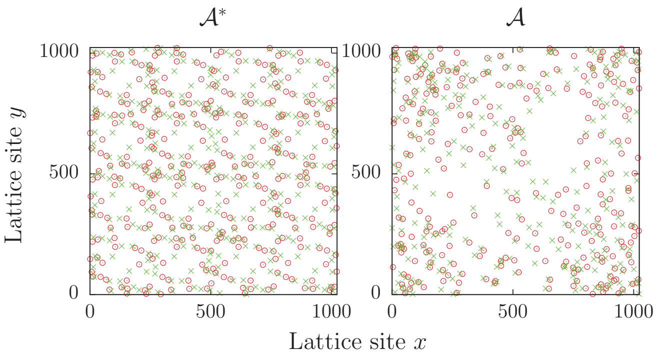

FIG. 8. (Color online) Vortex and antivortex positions shortly after turbulence creation at $t \simeq t_V$, for two single runs of the simulations on a grid of size $N_s = 1024$. Left: Initial condition $\mathcal{A}^*$. Right: Initial condition $\mathcal{A}$, as defined in Fig. 2.

for specific initial conditions $\mathcal{A}^*$ in the early-time stage. We attribute deviations from t^{-1} scaling during this period to an inhomogeneous distribution of vortices, encountered for certain initial conditions. To give an example, we show the vortex distributions created from the two initial conditions $\mathcal{A}^*$ and $\mathcal{A}$ in Fig. 8.

During the late-time stage, only a few vortices are bound in pairs, while most vortices are loosely bound and interact equally with a larger number of vortices around them. We heuristically take this into account by considering a modified scattering cross section $\sigma \sim l_D N_D^2$. The resulting kinetic equation reads $\partial_t N_V(t) \sim -N_V^4$, with solution $N_V(t) \sim t^{-1/3}$, and hence yields the reduction of the decay exponent observed at late times in our simulations.

G. Phase correlations

In the remainder of this article, we focus on the growth of long-range coherence at late times, associated with the annihilation of topological defects [17–22,42,43]. From this point of view, freely decaying superfluid turbulence is a particular example of phase-ordering dynamics after a quench into the ordered phase [73]. Whereas in three dimensions a second-order phase transition connects a normal fluid and a superfluid phase, a Bose gas in two dimensions experiences a BKT transition [45,46]. For the two-dimensional ultracold Bose gas, experimental and theoretical results support the understanding of the phase transition in terms of vortices undergoing an unbinding-binding transition [40,41,50,74–77].

In this context, we are interested in a comparison between correlation properties observed in the nonequilibrium dynamics near a NTFP and those known from equilibrium studies. We compute the dynamical trajectory of the vortex gas in the space of inverse coherence length and inverse mean vortex-antivortex pair distance. We compare our results to simulations of a thermal two-dimensional Bose gas specifically for our system parameters. For this, we evolve field configurations in time which are initially close to a thermal Rayleigh-Jeans distribution at a temperature T. After equilibration is reached, we compute the position of the states in the above phase space for different T.

We define a coherence length l_C in terms of the participation ratio [78] of the angle-averaged first-order coherence function $g^{(1)}(r) = \int d\theta \langle \phi^*(\mathbf{x})\phi(\mathbf{x}+\mathbf{r})\rangle / \sqrt{\langle n(\mathbf{x})\rangle \langle n(\mathbf{x}+\mathbf{r})\rangle}$,

$$l_C = \left(\mathcal{N} \int dr\, [g^{(1)}(r)]^2 \right)^{-1}, \qquad (7)$$

with $\mathcal{N} = [\int dr g^{(1)}(r)]^{-2}$. It measures the spatial extension of the first-order coherence function. Other than $r_{coh} = \int dr\, r^2 g^{(1)}(r) / \int dr\, r\, g^{(1)}(r)$, the quantity l_C does not sum up values of $g^{(1)}(r)$ weighted by the distance, which would enlarge insignificant contributions at large r. In addition, it gives meaningful results also in the case of large coherence $g^{(1)}(r) \simeq 1$, where, for instance, the FWHM measure cannot be applied any more. Note that in equilibrium this quantity smoothly interpolates between the regime of exponential decay of $g^{(1)}$ above the BKT transition, where the exponential coherence length ξ_C is defined as $g^{(1)}(r) \sim \exp(-r/\xi_C)$, and its power-law decay in the superfluid regime.

In Fig. 9, we follow the time evolution of the gas for $t > t_V$. One can observe that a state of low coherence and small mean vortex-antivortex pair distance evolves towards larger coherence and larger vortex-antivortex separation. As discussed in Secs. II B and II C, this is due to vortex annihilations and vortex-antivortex unbinding. For times $t > 10^4$, the coherence length grows as $l_C \sim \rho^{-1/2}$, in the same way as l_D shown in Fig. 5(b). The evolution considerably slows down

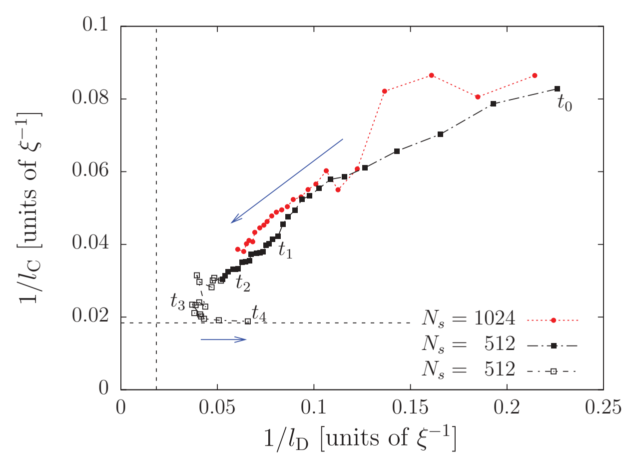

FIG. 9. (Color online) Trajectories of multivortex states in the space of inverse coherence length $1/l_C$ and inverse mean vortex-antivortex distance $1/l_D$, starting from $t = t_V$. Arrows are added to guide the eye along the time direction. Dashed lines mark the minimal values $2/L = 0.018\xi^{-1}$, available on a grid of size $N_s = 512$. Our understanding of the NTFP as a configuration with a few, maximally separated pairs on an otherwise maximally coherent background implies it to be located near the crossing of the dashed lines. Hence, the NTFP is approached most closely between $t \simeq 5 \times 10^5$ and $t \simeq 10^6 = t_3$. Filled (red) circles mark an average over 174 runs, $N_s = 1024$, initial time $t_V = 2.3 \times 10^3$, and final time $t_f = 1.3 \times 10^5$; filled squares, an average over 1223 runs, with $N_s = 512$, $t_V = 1.7 \times 10^3$, and $t_f = 2.6 \times 10^5$; and open squares, an average over 16 runs, $N_s = 512$, $t_i = 2.6 \times 10^5$, and $t_f = 4.2 \times 10^6$. Note that the symbols are equally spaced on a logarithmic time scale. We indicate the times $t_0 = 1.7 \times 10^3$, $t_1 = 1.6 \times 10^4$, $t_2 = 1.3 \times 10^5$, $t_3 = 1.0 \times 10^6$, and $t_4 = 4.2 \times 10^6$. The average number $N_V(t)$ of vortices left in the system is $N_V(t_0) = 97.7$, $N_V(t_1) = 21.8$, $N_V(t_2) = 11.7$, $N_V(t_3) = 5.8$, and $N_V(t_4) = 2.1$.

for $1/l_C \sim 1/l_D \to 0$. In this regime, the Bose gas shows characteristic scaling properties (see Refs. [16,24]), which indicate the presence of the NTFP [15]. After spending a long time near this point, the mean vortex-antivortex pair distance declines. This is a sign that the last remaining vortex-antivortex pairs reduce their size prior to their annihilation and the equilibration of the system. At about the same time the power law in the vortex density decay shown in Fig. 4 breaks down.

Our understanding of the NTFP as a configuration with a few, maximally separated pairs on an otherwise maximally coherent background implies it to be located near the crossing of the dashed lines. Hence, the NTFP is approached most closely between $t \simeq 5 \times 10^5$ and $t \simeq 10^6 = t_3$.

To set the above evolution in relation to equilibrium configurations, we show, in Fig. 10(a), the thermal line $[l_D^{-1}(T), l_C^{-1}(T)]$ for a range of temperatures T for which the system shows a nonvanishing zero-mode population. Note

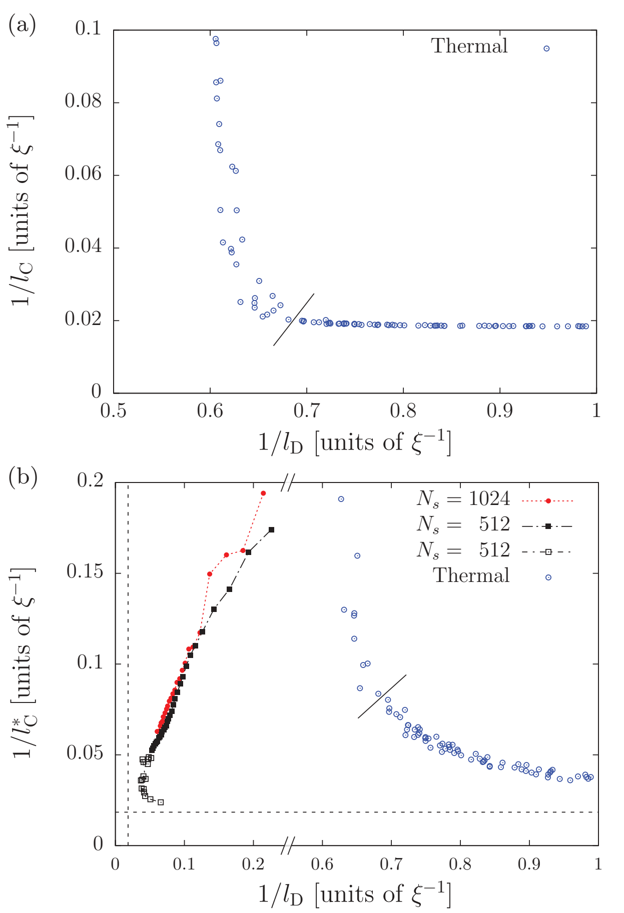

FIG. 10. (Color online) Multivortex states in the space of inverse coherence length and inverse mean vortex-antivortex distance. (a) Thermal configurations $[l_D^{-1}(T), l_C^{-1}(T)]$ for a range of temperatures T, increasing from bottom right to top left. The solid line marks the point where the decay of the $g^{(1)}(r)$ function changes from algebraic to exponential, signaling the BKT transition. (b) Comparison of the thermal line $[l_D^{-1}(T), l_C^{*-1}(T)]$ for the same range of temperatures T with the corresponding dynamical evolution. (Same data as in Fig. 9.) Dashed lines mark the minimal values $2/L = 0.018\xi^{-1}$, available on a grid of size $N_s = 512$. Note that the $(1/l_D)$ axis interval [0.25,0.55] has been cut out.

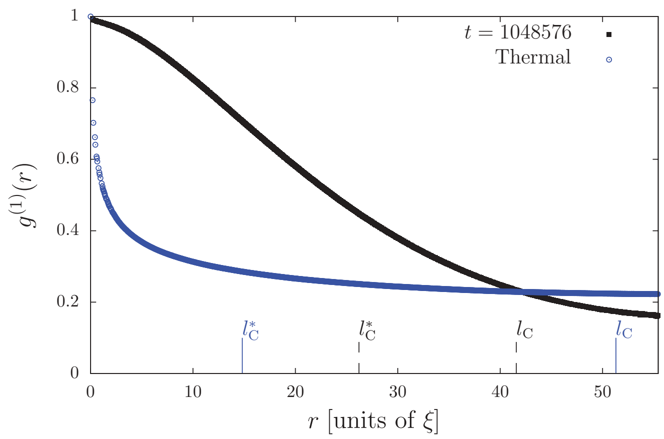

FIG. 11. (Color online) First-order coherence function $g^{(1)}$ as a function of radial coordinate r. We show one example for the system during the equilibration process at time $t = 1.05 \times 10^6$, with $l_C = 41.6\xi$, $l_C^* = 26.2\xi$, and one for a thermal configuration, giving $l_C = 51.3\xi$, $l_C^* = 14.8\xi$.

that, in order to define what counts as a bound vortex pair, we filter out field fluctuations on scales smaller than 0.55ξ before detecting vortices and antivortices. Hence, the resulting inverse of the mean vortex-antivortex pair distance represents a lower bound, and the separation of the NTFP from the thermal configurations becomes obvious.

In view of the thermal results it is useful to consider an alternative definition for the coherence length. The length $l_C^* = \int dr\, g^{(1)}(r)$ shares the above-mentioned advantages of the participation ratio. In addition, it does not overestimate the coherence of flat distributions. The thermal $g^{(1)}(r)$ functions show a fast decay at short distances r_s to a value $g_c^{(1)}$ and are almost constant for $r > r_s$. Figure 11 shows two typical $g^{(1)}$ functions, one for the system during the equilibration process at time $t = 1.05 \times 10^6$, with $l_C = 41.6\xi$, $l_C^* = 26.2\xi$, and one for a thermal configuration, giving $l_C = 51.3\xi$, $l_C^* = 14.8\xi$. Due to the small area under $g^{(1)}(r)$ up to r_s the normalization $\mathcal{N}$ in the definition of the participation ratio enlarges the integrand in Eq. (7) close to unity. Hence, l_C becomes large while l_C^* is less affected by this effect. In Fig. 10(b) we compare the thermal line $[l_D^{-1}(T), l_C^{*-1}(T)]$ for the same range of temperatures T with the corresponding dynamical evolution.

In Fig. 1, our findings are summarized qualitatively in a reduced phase space of the vortex gas. In this way, the "dynamical evolution" of decaying superfluid turbulence is compared to an estimate of the expected equilibrium configurations illustrated by the dashed line marked "thermal states," along which the temperature T varies. The most significant difference between these two lines is that the nonequilibrium dynamics is characterized by an increase in the mean vortex-antivortex pair distance with increasing coherence, whereas equilibrium configurations are expected to feature a decrease in pair distance with increasing coherence. A slowdown of the dynamics together with characteristic scaling of the single-particle momentum distribution, observed in the regime of large coherence and large vortex-antivortex pair distance, marks the position of the NTFP. Finally, when all vortices have annihilated, the system reaches the "thermal states" line deep in the superfluid regime.

III. CONCLUSIONS

We have studied the nonequilibrium dynamics of a two-dimensional dilute ultracold Bose gas towards and away from an NTFP. Following an initial quench, evolution towards a fixed point appears to be a generic feature of the (quasi-) condensation process and the buildup of coherence. In the course of a critically slowed evolution, vortex excitations evolved into an almost-random distribution reflected in the scaling of the single-particle spectra at the NTFP. We showed that the vortex-density decay is directly related to a nonequilibrium vortex unbinding process.

Our results allow us to draw a picture of the NTFP. The evolution path towards and away from the fixed point is summarized schematically in Fig. 1. There, we sketch the evolution of the multivortex states in the plane spanned by the coherence length l_C, defined in terms of the participation ratio, and the mean intervortex pair distance l_D. This picture allows us to compare our results with quasiequilibrium studies of a two-dimensional vortex gas. The NTFP emerges to bear similarities to the equilibrium BKT fixed point. The NTFP is characterized by a few pairs (in the extreme case, one pair) of far-separated anticirculating vortices. While the BKT transition also features unbinding of vortices, the finite temperature implies the simultaneous excitation of many rotons, i.e., strongly bound vortex-antivortex pairs. The NTFP is identified by strong wave turbulent scaling in the infrared limit [15], $n(k) \sim k^{-4}$. At the same time, the high-energy modes can be populated in a much weaker way, e.g., at a considerably lower temperature than the BKT critical temperature, or remain out of equilibrium. The details of the UV mode populations are determined by the way in which the NTFP is being approached. We emphasize that the approach of the NTFP is a generic but out-of-equilibrium process and that, eventually, the system will decay to an equilibrium state potentially far away from the NTFP. In the examples discussed in this paper, the total energy is sufficiently low that the final equilibrium state emerges to be considerably below the BKT critical temperature.

The way we force the system here (as in the work reported in [16,24]) to approach the NTFP generalizes the method of Kibble and Zurek. A strong sudden quench replaces the more or less adiabatic approach of the BKT phase transition. To what extent the BKT phase transition can be understood as happening within a class of thermal states near the NTFP studied here needs to be clarified by analyzing full out-of-equilibrium RG equations in comparison with standard descriptions in thermal equilibrium. We point out that the concept of an NTFP is far more general than the specific situation studied here (see, e.g., Refs. [15,25,27–30,32,33]).

Further important questions concern the relation to fully developed QT [5–12], which is believed to exhibit a quasiclassical Kolmogorov-Obukhov scaling [2,3] of the radial energy, $E(k) \sim k^{-5/3}$, in the infrared regime below the mean inverse distance between vortices [5–9]. In a recent experiment, a strong reduction of the vortex decay rate at late times has been reported [12]. Quantitative experimental observation of the predictions made here could provide new insight into the character of the NTFP and its relation to QT.

ACKNOWLEDGMENTS

The authors thank B. Anderson, J. Berges, N. G. Berloff, M. J. Davis, G. Krstulovic, J. M. Pawlowski, D. Sexty, B. Svistunov, and M. Tsubota for useful discussions. They acknowledge support by the Deutsche Forschungsgemeinschaft (GA677/7,8), by the University of Heidelberg (Excellence Initiative, Center for Quantum Dynamics), by the Helmholtz Association (HA216/EMMI), and by the University of Leipzig (Grawp-Cluster).

APPENDIX: QUANTUM HYDRODYNAMIC ENERGY DECOMPOSITION

In this Appendix we give details on the energy decomposition introduced in Refs. [5,59]. To exhibit vortical flow and define the decomposition we use the polar representation $\phi(\mathbf{x},t) = \sqrt{n(\mathbf{x},t)}\exp\{i\varphi(\mathbf{x},t)\}$ of the field in terms of the density $n(\mathbf{x},t)$ and a phase angle $\varphi(\mathbf{x},t)$. This allows us to express the particle current $\mathbf{j} = i(\phi^*\nabla\phi - \phi\nabla\phi^*)/2 = n\mathbf{v}$ in terms of the velocity field $\mathbf{v} = \nabla\varphi$. With this, we decompose the kinetic-energy spectrum following Refs. [5,59], splitting the total kinetic energy $E_{\text{kin}} = \int d^dx\, \langle|\nabla\phi(\mathbf{x},t)|^2\rangle/(2m)$ as $E_{\text{kin}} = E_{\text{v}} + E_{\text{q}}$ into a "classical" part and a "quantum-pressure" component,

$$E_{\text{v}} = \frac{1}{2m}\int d^dx\, \langle|\sqrt{n}\mathbf{v}|^2\rangle, \tag{A1}$$

$$E_{\text{q}} = \frac{1}{2m}\int d^dx\, \langle|\nabla\sqrt{n}|^2\rangle\,. \tag{A2}$$

The radial energy spectra for these fractions involve the Fourier transform of the generalized velocities $\mathbf{w}_{\text{v}} = \sqrt{n}\mathbf{v}$ and $\mathbf{w}_{\text{q}} = \nabla\sqrt{n}$,

$$E_\delta(k) = \frac{1}{2m}\int k^{d-1}d\Omega_d\, \langle|\mathbf{w}_\delta(\mathbf{k})|^2\rangle, \quad \delta = \text{v},\text{q}. \tag{A3}$$

Following Refs. [5,59], the velocity $\mathbf{w}_{\text{v}}$ is, furthermore, decomposed into "incompressible" (divergence-free) and "compressible" (solenoidal) parts, $\mathbf{w}_{\text{v}} = \mathbf{w}_{\text{i}} + \mathbf{w}_{\text{c}}$, with $\nabla\cdot\mathbf{w}_{\text{i}} = 0$, $\nabla\times\mathbf{w}_{\text{c}} = 0$, to distinguish vortical superfluid and rotationless motion of the fluid.

[1] L. F. Richardson, Proc. R. Soc. London A **97**, 354 (1920).
[2] A. N. Kolmogorov, Proc. USSR Acad. Sci. **30**, 299 (1941) [Proc. R. Soc. Lond. A **434**, 9 (1991)].
[3] A. M. Obukhov, Izv. Akad. Nauk SSSR, Ser. Geogr. Geofiz. **5**, 453 (1941).
[4] U. Frisch, *Turbulence: The Legacy of A. N. Kolmogorov* (Cambridge University Press, Cambridge, UK, 1995).
[5] C. Nore, M. Abid, and M. E. Brachet, Phys. Rev. Lett. **78**, 3896 (1997).

[6] W. F. Vinen and J. J. Niemela, J. Low Temp. Phys. **128**, 167 (2002).
[7] T. Araki, M. Tsubota, and S. K. Nemirovskii, Phys. Rev. Lett. **89**, 145301 (2002).
[8] M. Kobayashi and M. Tsubota, Phys. Rev. Lett. **94**, 065302 (2005).
[9] D. Proment, S. Nazarenko, and M. Onorato, Physica D **241**, 304 (2011).
[10] E. A. L. Henn, J. A. Seman, G. Roati, K. M. F. Magalhães, and V. S. Bagnato, Phys. Rev. Lett. **103**, 045301 (2009).
[11] J. Seman *et al.*, Las. Phys. Lett. **8**, 691 (2011).
[12] T. W. Neely *et al.*, arXiv:1204.1102 [cond-mat.quant-gas].
[13] V. E. Zakharov, V. S. L'vov, and G. Falkovich, *Kolmogorov Spectra of Turbulence I: Wave Turbulence* (Springer-Verlag, Berlin, 1992).
[14] S. Nazarenko, *Wave Turbulence*, *Lecture Notes in Physics No. 825* (Springer-Verlag, Heidelberg, 2011).
[15] C. Scheppach, J. Berges, and T. Gasenzer, Phys. Rev. A **81**, 033611 (2010).
[16] B. Nowak, D. Sexty, and T. Gasenzer, Phys. Rev. B **84**, 020506(R) (2011).
[17] E. Levich and V. Yakhot, J. Phys. A: Math. Gen. **11**, 2237 (1978).
[18] Y. Kagan, B. V. Svistunov, and G. V. Shlyapnikov, Zh. Eksp. Teor. Fiz. **101**, 528 (1992) [Sov. Phys. JETP **74**, 279 (1992)].
[19] Y. Kagan and B. V. Svistunov, Zh. Eksp. Teor. Fiz. **105**, 353 (1994) [Sov. Phys. JETP **78**, 187 (1994)].
[20] N. G. Berloff and B. V. Svistunov, Phys. Rev. A **66**, 013603 (2002).
[21] B. Svistunov, in *Quantized Vortex Dynamics and Superfluid Turbulence*, *Lecture Notes in Physics No. 571*, edited by C. Barenghi, R. Donnelly, and W. Vinen (Springer-Verlag, Berlin, 2001).
[22] E. V. Kozik and B. V. Svistunov, J. Low Temp. Phys. **156**, 215 (2009).
[23] Y. Kagan and B. V. Svistunov, Phys. Rev. Lett. **79**, 3331 (1997).
[24] B. Nowak, J. Schole, D. Sexty, and T. Gasenzer, Phys. Rev. A **85**, 043627 (2012).
[25] M. Schmidt, S. Erne, B. Nowak, D. Sexty, and T. Gasenzer, New J. Phys. **14**, 075005 (2012).
[26] R. Micha and I. I. Tkachev, Phys. Rev. Lett. **90**, 121301 (2003).
[27] J. Berges, A. Rothkopf, and J. Schmidt, Phys. Rev. Lett. **101**, 041603 (2008).
[28] J. Berges and G. Hoffmeister, Nucl. Phys. B **813**, 383 (2009).
[29] J. Berges and D. Sexty, Phys. Rev. D **83**, 085004 (2011).
[30] T. Gasenzer, B. Nowak, and D. Sexty, Phys. Lett. B **710**, 500 (2012).
[31] P. B. Arnold and G. D. Moore, Phys. Rev. D **73**, 025006 (2006); **73**, 025013 (2006).
[32] J. Berges, S. Scheffler, and D. Sexty, Phys. Lett. B **681**, 362 (2009).
[33] M. Carrington and A. Rebhan, Eur. Phys. J. C **71**, 1787 (2011).
[34] J.-P. Blaizot, F. Gelis, J.-F. Liao, L. McLerran, and R. Venugopalan, Nucl. Phys. A **873**, 68 (2012).
[35] J. Berges and D. Sexty, Phys. Rev. Lett. **108**, 161601 (2012).
[36] K. Fukushima and F. Gelis, Nucl. Phys. A **874**, 108 (2012).
[37] K. Fukushima, Acta Phys. Pol. B **42**, 2697 (2011).
[38] P. C. Hohenberg and B. I. Halperin, Rev. Mod. Phys. **49**, 435 (1977).
[39] C. Timm, Physica C: Superconductivity **265**, 31 (1996).
[40] R. N. Bisset, M. J. Davis, T. P. Simula, and P. B. Blakie, Phys. Rev. A **79**, 033626 (2009).
[41] C. J. Foster, P. B. Blakie, and M. J. Davis, Phys. Rev. A **81**, 023623 (2010).
[42] K. Damle, S. N. Majumdar, and S. Sachdev, Phys. Rev. A **54**, 5037 (1996).
[43] S. Nazarenko and M. Onorato, Physica D: Nonlin. Phen. **219**, 1 (2006).
[44] L. Onsager, Nuovo Cim. Suppl. **6**, 279 (1949).
[45] V. Berezinskii, Sov. J. Exp. Theor. Phys. **32**, 493 (1971).
[46] J. Kosterlitz and D. Thouless, J. Phys. C **6**, 1181 (1973).
[47] T. W. B. Kibble, J. Phys. A: Math. Gen. **9**, 1387 (1976).
[48] W. H. Zurek, Nature **317**, 505 (1985).
[49] L. Mathey, K. Günter, J. Dalibard, and A. Polkovnikov, arXiv:1112.1204 [cond-mat.quant-gas].
[50] C. N. Weiler, T. W. Neely, D. R. Scherer, A. S. Bradley, M. J. Davis, and B. P. Anderson, Nature **455**, 948 (2008).
[51] G. Eyink and N. Goldenfeld, Phys. Rev. E **50**, 4679 (1994).
[52] L. Mathey and A. Polkovnikov, Phys. Rev. A **80**, 041601 (2009); **81**, 033605 (2010).
[53] A. Mitra and T. Giamarchi, Phys. Rev. Lett. **107**, 150602 (2011); Phys. Rev. B **85**, 075117 (2012).
[54] L. Canet and H. Chate, J. Phys. A **40**, 1937 (2007).
[55] T. Gasenzer and J. M. Pawlowski, Phys. Lett. B **670**, 135 (2008).
[56] T. Gasenzer, S. Kessler, and J. M. Pawlowski, Eur. Phys. J. C **70**, 423 (2010).
[57] For videos of the evolution, see [http://www.thphys.uni-heidelberg.de/∼smp/gasenzer/videos/boseqt.html].
[58] H. Aref, Annu. Rev. Fluid Mech. **15**, 345 (1983).
[59] C. Nore, M. Abid, and M. E. Brachet, Phys. Fluids **9**, 2644 (1997).
[60] G. Krstulovic and M. Brachet, Phys. Rev. E **83**, 066311 (2011).
[61] V. Ambegaokar, B. I. Halperin, D. R. Nelson and E. D. Siggia, Phys. Rev. B **21**, 1806 (1980).
[62] G. F. Carnevale, J. C. McWilliams, Y. Pomeau, J. B. Weiss, and W. R. Young, Phys. Rev. Lett. **66**, 2735 (1991).
[63] J. B. Weiss and J. C. McWilliams, Phys. Fluids A **3**, 608 (1993).
[64] A. Bracco, J. C. McWilliams, G. Murante, A. Provenzale, and J. B. Weiss, Phys. Fluids **12**, 2931 (2000).
[65] P. Tabeling, S. Burkhart, O. Cardoso, and H. Willaime, Phys. Rev. Lett. **67**, 3772 (1991).
[66] R. Benzi, M. Colella, M. Briscolini, and P. Santangelo, Phys. Fluids A **4**, 1036 (1992).
[67] C. Sire, P.-H. Chavanis, and J. Sopik, Phys. Rev. E **84**, 056317 (2011).
[68] C. Sire and P.-H. Chavanis, Phys. Rev. E **61**, 6644 (2000).
[69] V. Yakhot and J. Wanderer, Phys. Rev. Lett. **93**, 154502 (2004).

[70] H.-C. Chu and G. A. Williams, Phys. Rev. Lett. **86**, 2585 (2001).
[71] S. Nazarenko and M. Onorato, J. Low Temp. Phys. **146**, 31 (2007).
[72] R. Numasato, M. Tsubota, and V. S. L'vov, Phys. Rev. A **81**, 063630 (2010).
[73] A. J. Bray, Adv. Phys. **43**, 357 (1994).
[74] Z. Hadzibabic, P. Krüger, M. Cheneau, B. Battelier, and J. Dalibard, Nature **441**, 1118 (2006).
[75] T. P. Simula and P. B. Blakie, Phys. Rev. Lett. **96**, 020404 (2006).
[76] V. Schweikhard, S. Tung, and E. A. Cornell, Phys. Rev. Lett. **99**, 030401 (2007).
[77] L. Giorgetti, I. Carusotto, and Y. Castin, Phys. Rev. A **76**, 013613 (2007).
[78] B. Kramer and A. MacKinnon, Rep. Progr. Phys. **56**, 1469 (1993).